

PAPER

## Two-dimensional kinetic analysis of a Hall thruster discharge with a null-magnetic point at the anode

To cite this article: A Marín-Cebrián *et al* 2025 *J. Phys. D: Appl. Phys.* **58** 375201

View the [article online](#) for updates and enhancements.

### You may also like

- [Thickness-driven structural and magnetic evolution in permalloy thin films](#)

Karthik Krishnan, Kapil Dev, Shubham Kumar et al.

- [Wind tunnel experiments of long arcs in crossflow: anodic roots and influence of flow field](#)

Fayleon Lin, Vincent Andraud, Guillem Tobella et al.

- [Electric field modulation and hot-electron suppression in AlGaN/GaN HEMTs on Si using a hybrid p-NiO RESURF-FP termination](#)

Ruiling Gong, Hui Guo, Junyang An et al.



EDINBURGH  
INSTRUMENTS

### FLS1000 MULTIMODAL PHOTOLUMINESCENCE SPECTROMETER

- + Photoluminescence Spectra, Lifetime, and Quantum Yield in One Instrument
- + Ultimate Sensitivity: Signal-To-Noise Ratio 35,000:1
- + Modular and Customisable to your Application
- + Advanced Accessories: Micro-Spectroscopy, X-Ray Excitation, Circularly Polarised Luminescence (CPL)



Discover the FLS1000

VISIT OUR WEBSITE FOR MORE DETAILS

MADE IN THE UK

edinst.com

# Two-dimensional kinetic analysis of a Hall thruster discharge with a null-magnetic point at the anode

A Marín-Cebrián<sup>1,\*</sup> , E Ahedo<sup>1</sup>  and A Domínguez-Vázquez<sup>2</sup> 

<sup>1</sup> Department of Aerospace Engineering, Universidad Carlos III de Madrid, Leganés, Spain

<sup>2</sup> Department of Mechanical, Thermal and Fluid Engineering, Universidad de Málaga, Málaga, Spain

E-mail: [almarinc@pa.uc3m.es](mailto:almarinc@pa.uc3m.es)

Received 13 June 2025, revised 8 August 2025

Accepted for publication 19 August 2025

Published 10 September 2025



## Abstract

A two-dimensional axial-radial particle-in-cell model is used to analyze the electron response in a non-shielded 5 kW class Hall thruster. Radial asymmetries in the plasma discharge are present due to the cylindrical thruster geometry and the magnetic topology. The applied magnetic field presents a near-null point at the anode, from which a magnetic separatrix (MS) is born.

Downstream of the MS, the plasma response is standard for a magnetic lens topology and agrees well with previous studies. In contrast, upstream of the MS, the magnetic field is nearly axial and partially shields the lateral walls. The magnetized electrons cannot easily cross the MS and are channeled toward the near-null magnetic point at the anode. This leads to sharp changes in the bulk plasma properties, significantly decreasing particle and energy fluxes to the walls.

The lack of electrons reaching the outer dielectric wall upstream of the MS leads to the collapse of the classical electron-repelling sheath structure in order to comply with the dielectric condition. Electrons in this region are heated, and their inertia becomes comparable to their thermal energy. Moreover, consistently with previous simulations assuming a radial magnetic field, the electron response differs from a collisional fluid in terms of wall interaction properties, heat flux, and finite Larmor radius effects.

Keywords: Hall thruster, particle-in-cell, curved magnetic topology, kinetic electron response

## 1. Introduction

The complex physics involved in the Hall effect thruster (HET) plasma is still not fully understood [1], hindering the development of accurate and efficient models of the discharge. Currently, simulations of real thrusters rely mainly on axial-radial quasineutral hybrid models [2–5] due to their good trade-off between computational cost and accuracy. These models treat heavy species (i.e. ions and neutrals) with a particle-in-cell (PIC) formulation and electrons as a drift-diffusive fluid. The standard electron fluid formulation assumes a (near) Maxwellian velocity distribution function

(VDF) [6]. However, the low collisionality in the HET channel prevents the plasma from reaching local thermodynamic equilibrium; and thus, standard fluid models can misrepresent some relevant phenomena [7]. In particular, deviations of the electron VDF from the equilibrium Maxwellian modify the macroscopic response, particle and energy fluxes to the walls. Therefore, a precise characterization of the electron dynamics is essential to evaluate the discharge performance. In this context, full PIC models [8], capable of resolving the electron VDF, are used to investigate the electron dynamics and can enrich electron fluid models with valuable kinetic information.

The analysis of the electron dynamics with PIC models in scenarios with a purely radial magnetic field [9–14] has revealed important differences with respect to standard fluid models. In particular: (1) the electron VDF departs largely

\* Author to whom any correspondence should be addressed.

from the Maxwellian, (2) plasma-wall interaction parameters can differ largely from classical theory, (3) the electron heat flux has a complex behavior and, in general, it cannot be described by a Fourier-type law, and (4) the pressure tensor is composed of a gyrotropic anisotropic part and small gyroviscous terms. Indeed, near the anode, gyroviscosity, and electron inertia (i.e. finite Larmor radius effects, FLR) are relevant in the azimuthal momentum equation, where dominant terms are two orders of magnitude smaller than those in the axial momentum equation.

However, the magnetic field in real HETs is curved. A magnetic lens topology is used to reduce the detrimental plasma fluxes to the lateral walls and improve the thruster performance [15–17]. Previous studies using 1D PIC models [18, 19] have discussed the effect of the magnetic field curvature on the plasma response. The kinetic solution shows a significant reduction in electron temperature anisotropy and a higher replenishment of the wall collectible electron VDF tail. Axial-radial 2D models overcome some of the inherent limitations of 1D models and are more appropriate to analyze scenarios with complex magnetic topologies. Previous axial-radial 2D PIC simulation with a curved magnetic field topology mainly focused on the analysis of the ion species and the characterization of thruster performance figures [20–24], while few of them have been devoted to study the electron response [25].

In this work, we use our 2D axial-radial PIC model (PICASO) [14] to analyze the effect of the magnetic field curvature on the plasma response, with special emphasis on the electron dynamics. A 5 kW-class HET similar to a PPS5000 [26, 27], with a non-shielded magnetic topology is considered for this study. The magnetic field features a near-null magnetic point at the anode wall (a similar magnetic topology can be found in [28–30]) and partially shields the lateral walls of the annular channel in the near-anode region. Results include the analysis of the VDFs, macroscopic transport equations, and plasma-wall interaction magnitudes. It is shown that the peculiar magnetic topology yields an unconventional electron response in the near-anode region.

The article is structured as follows. Section 2 summarizes the main aspects of the kinetic model. Section 3 presents the macroscopic plasma response and the species VDF. Plasma-wall interaction magnitudes are commented in section 4. Section 5 analyzes the continuity, momentum, and energy equations of electrons, revealing the leading contributions in the macroscopic transport equations. Section 6 discusses the local plasma response near the anode. Finally, conclusions are gathered in section 7. Preliminary results of this work were presented at the 38th International Electric Propulsion Conference [31].

## 2. Thruster configuration and kinetic model

Figure 1(a) shows the simulation domain, comprising the thruster channel and the near plume. The domain boundaries

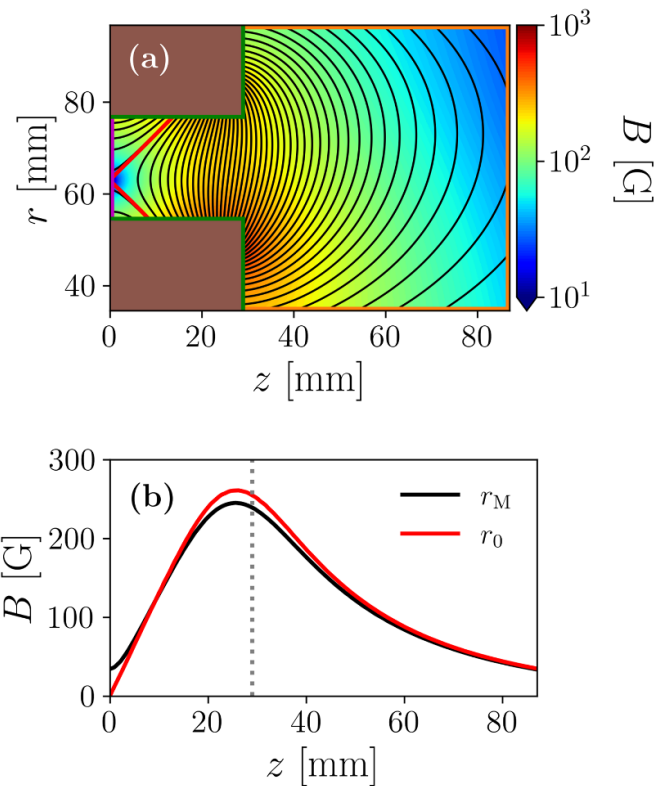


**Figure 1.** Simulation domain and magnetic field topology. (a) 2D map of the magnitude of the applied magnetic field; magnetic field lines (—), the MS (—), the anode surface (A) (—), dielectric walls (W) (—), and the neutralizer/plume boundary (N) (—). (b) Axial profiles of  $B = |\mathbf{B}|$  at  $r = r_M = 65.6$  mm and at  $r = r_0 = 62.9$  mm.

are defined by the metallic anode (A), the lateral dielectric thruster walls (W), and the downstream plume boundary, which acts as a cathode/neutralizer (N). The thruster chamber has a length of  $L = 29$  mm, and inner and outer radii  $r_{W1} = 54.5$  mm and  $r_{W2} = 76.7$  mm. The channel mean radius is  $r_M = 65.6$  mm. The plume extends up to two channel lengths along the axial direction, and approximately three channel widths along the radial direction. Previous simulations [31] have shown that the plume size is large enough not to modify the results inside the HET channel.

Figure 1(a) also depicts the 2D map of the magnitude of the applied, static magnetic field,  $\mathbf{B}$ . On the anode wall, at  $r = r_0 = 62.9$  mm, there is a near-null point of the magnetic field (minimum  $B = |\mathbf{B}|$  is 0.2 G), and from there a magnetic separatrix (MS) is born. The MS intersects the inner wall at  $z \approx 8.46$  mm, and the outer wall at  $z \approx 13.65$  mm. Thus, the MS separates the channel volume into three regions: the one downstream is rather conventional with a magnetic lens topology and  $B_r$  dominating; then there are two ‘triangular’ regions between the MS and anode, with highly-curved magnetic lines, dominated by  $B_z$ , which intersect near perpendicularly the anode and confine

magnetically the lateral walls. Cylindrical asymmetries are also evident in the magnetic field map. Axial profiles of  $B$  at  $r = r_M$  and  $r = r_0$  are plotted in figure 1(b).

In this work, the axisymmetric model PICASO [14] simulates electrons ( $e$ ) and singly-charged xenon ions ( $i$ ) with a PIC formulation as two different populations of macroparticles with constant weight (i.e. number of elementary particles per simulated macroparticle). Explicit time integration of particle trajectories uses the Boris algorithm [32] and cylindrical effects on the particle motion are considered as described in [33]. First-order weighting schemes (Cloud-In-Cell) are used for both, interpolating the magnetic and electric field to the particle position, and calculating the VDF of each species as well as their macroscopic magnitudes.

The main macroscopic magnitudes of interest for species  $s$  are the density  $n_s$ , the particle flux vector  $n_s \mathbf{u}_s$ , the momentum flux tensor  $\bar{\bar{M}}_s$ , and the energy flux vector  $\mathbf{P}_s''$ , defined as

$$\begin{aligned} n_s &= \iiint f_s d^3v, \quad n_s \mathbf{u}_s = \iiint \mathbf{v} f_s d^3v, \\ \bar{\bar{M}}_s &= m_s \iiint \mathbf{v} v f_s d^3v, \quad \mathbf{P}_s'' = \frac{m_s}{2} \iiint v \mathbf{v}^2 f_s d^3v. \end{aligned} \quad (1)$$

The implemented weighting algorithm is described in detail in the appendix of [14]. Other related macroscopic magnitudes are the current density vector  $\mathbf{j}_s = e Z_s n_s \mathbf{u}_s$ , the pressure tensor  $\bar{\bar{p}}_s = \bar{\bar{M}}_s - m_s n_s \mathbf{u}_s \mathbf{u}_s$ , the directional temperatures  $T_{xs} = p_{xxs}/n_s$  for  $x = z, r, \theta$ , and the scalar temperature  $T_s = \text{trace}(\bar{\bar{p}}_s)/(3n_s)$ . The time-averaged macroscopic magnitudes at steady-state are calculated through the Extended Volumetric Weighting algorithm, described in section 3.2 of [12].

Since our main focus is electron dynamics, in order to limit the computational cost, we avoid simulating the slow dynamics of neutrals ( $n$ ). Following [14], we model the neutral density with the simplified depletion law,

$$n_n(z) = \frac{\dot{m} - \dot{m}_{zi}(z)}{u_{zn} A m_i}, \quad (2)$$

where  $m_i$  is the ion mass,  $A$  is the channel cross-section area,  $u_{zn}$  is the (constant) neutral axial fluid velocity,  $\dot{m}_{zi}(z)$  is the axial ion mass flow (computed at each axial section of the thruster) and  $\dot{m}$  is the injected neutral mass flow through the anode. Equation (2) conserves the total mass flow and accounts for both, volumetric ionization and recombination of ions reaching the thruster walls. This approach avoids neutral dynamics, such as the breathing mode, and can be considered valid if the plasma response is steady-state.

Elastic, excitation, and ionization collisions of electrons with neutrals are treated with standard Monte Carlo collision algorithms. Ion collisions are quite marginal inside the thruster and are neglected in this work. Collisional cross-sections are retrieved from the Biagi database available in LXC at [34]. Due to the axial-radial nature of the simulation, azimuthal instabilities inducing cross-field electron transport cannot be

resolved. Instead, an empirical diffusive model is implemented through an isotropic anomalous electron collisionality of the form  $\nu_{\text{ano}} = \alpha_{\text{ano}} \omega_{ce}$ , with  $\omega_{ce} = eB/m_e$  the electron cyclotron frequency and  $\alpha_{\text{ano}}$  a two-parameter step function.

Electron and ion particles reaching any domain boundary contribute to the electric current there and are then removed from the simulation. The anode and cathode are connected through a power source setting a constant voltage bias  $V_d$  and with a (time-dependent) discharge current  $I_d(t)$ . At any instant, electrons are uniformly injected through the cathode surface, sampled from a Maxwellian flux VDF with a mean energy of 4.5 eV, such that the instantaneous net electric current at the anode and cathode are the same. Secondary electron emission (SEE) from the dielectric walls is taken into account, following the linear SEE yield

$$\delta_s(\mathcal{E}_{ewt}) = \mathcal{E}_{ewt}/\mathcal{E}_c, \quad (3)$$

with  $\mathcal{E}_{ewt}$  the impacting electron energy and  $\mathcal{E}_c$  the material cross-over energy. In the simulations here:  $\mathcal{E}_c = 50$  eV and secondary electrons are sampled from a Maxwellian flux VDF with an average energy of 0.4 eV.

In the electrostatic approximation the electric field is  $\mathbf{E} = -\nabla\phi$  and the electric potential,  $\phi$ , is obtained from the Poisson equation

$$\frac{\partial^2 \phi}{\partial z^2} + \frac{\partial^2 \phi}{\partial r^2} + \frac{1}{r} \frac{\partial \phi}{\partial r} = \frac{e(n_e - n_i)}{\epsilon}, \quad (4)$$

where  $\epsilon$  is the electric permittivity and  $n_e$ ,  $n_i$  are the electron and ion densities respectively. Dirichlet conditions are imposed at the cathode and anode,  $\phi_N = 0$  and  $\phi_A = V_d$ , and Neumann conditions are applied at the dielectric walls,

$$\epsilon \mathbf{E} \cdot \mathbf{1}_n = \sigma(t) \equiv - \int_0^t \mathbf{j} \cdot \mathbf{1}_n dt, \quad (5)$$

where:  $\mathbf{1}_n$  is the unit vector perpendicular to the surface and pointing towards the plasma,  $\sigma$  is the surface charge density, and  $\mathbf{j}$  is the electric current density. At the steady-state equation (5) yields a local zero current at the dielectric walls. The numerical implementation of equation (4) makes use of second-order finite differences at the mesh nodes and the resulting set of linear equations is solved using the direct PARDISO solver included in the Math Kernel Library of INTEL [35].

The strict numerical constraints on the cell size and time step imposed by the Debye length and the inverse plasma frequency, respectively, are relaxed by using an augmented permittivity  $\epsilon = f_D^2 \epsilon_0$ , where  $\epsilon_0$  is the vacuum permittivity. This allows a reduction of the computational cost by a factor  $f_D^2$  without a significant distortion of the steady-state solution as long as the Debye length remains the smallest length scale of the problem [14].

A single operation point with  $V_d = 300$  V,  $\dot{m} = 17.59 \text{ mg s}^{-1}$ , and  $u_{zn} = 300 \text{ m s}^{-1}$  is simulated. Empirical

parameters for the anomalous transport model were taken from [36] featuring  $\alpha_{\text{ano},1} = 1.2\%$  and  $\alpha_{\text{ano},2} = 4.8\%$  for the inner and outer anomalous transport coefficients. The numerical simulation presented here uses  $f_D = 12$ , a value aligned with previous works in the literature [21, 23]. For  $n_e = 3 \cdot 10^{18} \text{ m}^{-3}$ ,  $T_e = 20 \text{ eV}$ , and  $B = 250 \text{ G}$  as typical values, the following characteristic plasma magnitudes are computed: (augmented) Debye length  $\lambda_{\text{De}} = 230 \mu\text{m}$ ; electron Larmor radius,  $\rho_e = 681 \mu\text{m}$ ; (augmented) inverse plasma frequency  $\omega_{pe}^{-1} = 123 \text{ ps}$ ; and inverse electron gyrofrequency,  $\omega_{ce}^{-1} = 227 \text{ ps}$ . The domain discretization uses a mesh with square cells with a length of  $200 \mu\text{m}$ . The PIC time-step is  $\Delta t = 15 \text{ ps}$  and the total simulated time is  $60 \mu\text{s}$  (i.e. 4 million timesteps). The effect of the numerical parameters on the plasma solution is addressed in the appendix, confirming the robustness of the results. Simulations were run on a workstation with 2 sockets, each one with 20 cores Intel(R) Xeon(R) Gold 6230 CPU @ 2.10 GHz. Using 20 cores, the reference simulation took approximately 169h.

### 3. First simulation results

The simulation starts with the domain uniformly filled with Maxwellian VDFs of ions and electrons, with densities and temperatures  $n_{e0} = n_{i0} = 4 \cdot 10^{17} \text{ m}^{-3}$  and  $T_{e0} = T_{i0} = 1 \text{ eV}$ . During the initial transient, electrons and ions reaching the walls build up the surface charge density according to equation (5). Debye sheaths develop until the electric current to the wall becomes zero. The surface charge and the sheath stabilize after  $\sim 0.5 \mu\text{s}$ . Other transient processes related to ion dynamics and described in [14] follow until the steady state is reached at about  $40 \mu\text{s}$ . Figure 2 illustrates the transient period with the global currents at the outer dielectric wall. Hereon, only the stationary plasma response is shown and discussed. To mitigate the PIC-related noise, the plotted results are time-averaged values over the last  $7.5 \mu\text{s}$  of the simulation (i.e. half a million time-steps). At steady state, the number of simulated particles per species,  $N_p$ , is over one million.

Figure 3 shows 2D maps of the main macroscopic plasma magnitudes. Three regions can be distinguished: (1) the near-plume region outside the thruster, (2) the thruster near-exit region, and (3) the thruster near-anode region. The first notable feature in the maps is the presence of cylindrical asymmetries, arising from both, the geometry and the magnetic configuration; see, for instance, the ion and electron longitudinal currents in the plume (for vector magnitudes, such as  $j_e$ , the longitudinal part is defined as  $\tilde{j}_e = j_e - j_{\theta e} \mathbf{1}_\theta$ ). In this paper, the analysis focuses on the thruster channel plasma, which reveals significant differences between the regions upstream and downstream of the MS. The plasma magnitudes in the near-exit region are quite standard: a maximum  $T_e$  around the thruster exit; a maximum  $n_e$  inside the thruster, just when  $\phi$  starts to decrease axially (thus accelerating ions); and a radial decay of  $\phi$ . On the contrary, the near-anode region presents

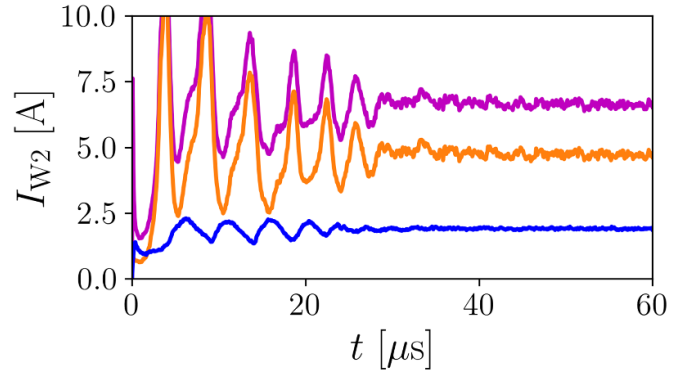


**Figure 2.** Time evolution of the electron and ion currents to the outer wall: ions reaching the wall,  $|I_{iW2}|$  (blue), electrons reaching the wall,  $|I_{eW2t}|$  (magenta), and electrons emitted from the wall (SEE),  $|I_{eW2f}|$  (orange).

peculiar and complex features that we will analyze in detail in section 6.

Moving to the kinetic description, figure 4 plots the normalized 1D electron VDFs at  $r = r_0$  and different axial positions inside the HET channel. These 1D VDFs are defined as

$$\hat{f}_e^{(z)}(v_z) = \iint_{-\infty}^{\infty} f_e(\mathbf{v}) dv_r dv_\theta \quad (6)$$

and similarly for  $\hat{f}_e^{(r)}(v_r)$  and  $\hat{f}_e^{(\theta)}(v_\theta)$ . The plots use the directional electron energy in the horizontal axis and a logarithmic scale in the vertical axis. Therefore, a Maxwellian VDF yields a line with a constant slope, and the wider the VDF, the higher the directional temperature. The relative shapes of the VDFs in figure 4 illustrate the axial decrease of  $T_e$  from channel exit to anode, in agreement with figure 3(b). The resulting electron VDF behavior differs depending on the thruster region. Near the thruster exit, at  $z = 25 \text{ mm}$  at  $z = 15 \text{ mm}$ , the axial and azimuthal VDF are almost identical with an approximately linear slope, yielding  $T_{ze} \simeq T_{\theta e}$ . The weak asymmetry between  $\hat{f}_e^{(z)}$  and  $\hat{f}_e^{(\theta)}$  is due to  $u_{ze} \ll u_{\theta e} \ll c_e$ . The high energy tails of the radial VDF are depleted due to wall collection and the weak electron collisionality. This reduces the radial temperature and leads to temperature anisotropy with  $T_{re} < T_{ze} \simeq T_{\theta e}$ . Qualitatively, this result is identical to those obtained from previous 1Dr models of the acceleration region of the discharge [12, 37] assuming a purely radial magnetic field. As we move towards the central part of the channel, the magnetic curvature increases. At  $z = 9 \text{ mm}$  it can be observed a higher replenishment of the radial VDF. This result is in agreement with previous works with 1D models accounting for the magnetic field curvature [18, 19], which explained this effect due to the larger mixing between the radial and axial components of the velocity as a consequence of the magnetic field shape. At  $z = 6 \text{ mm}$  the low wall losses [see section 4] and high curvature of the magnetic field leads to  $\hat{f}_e^{(r)}$  not presenting depleted tails.

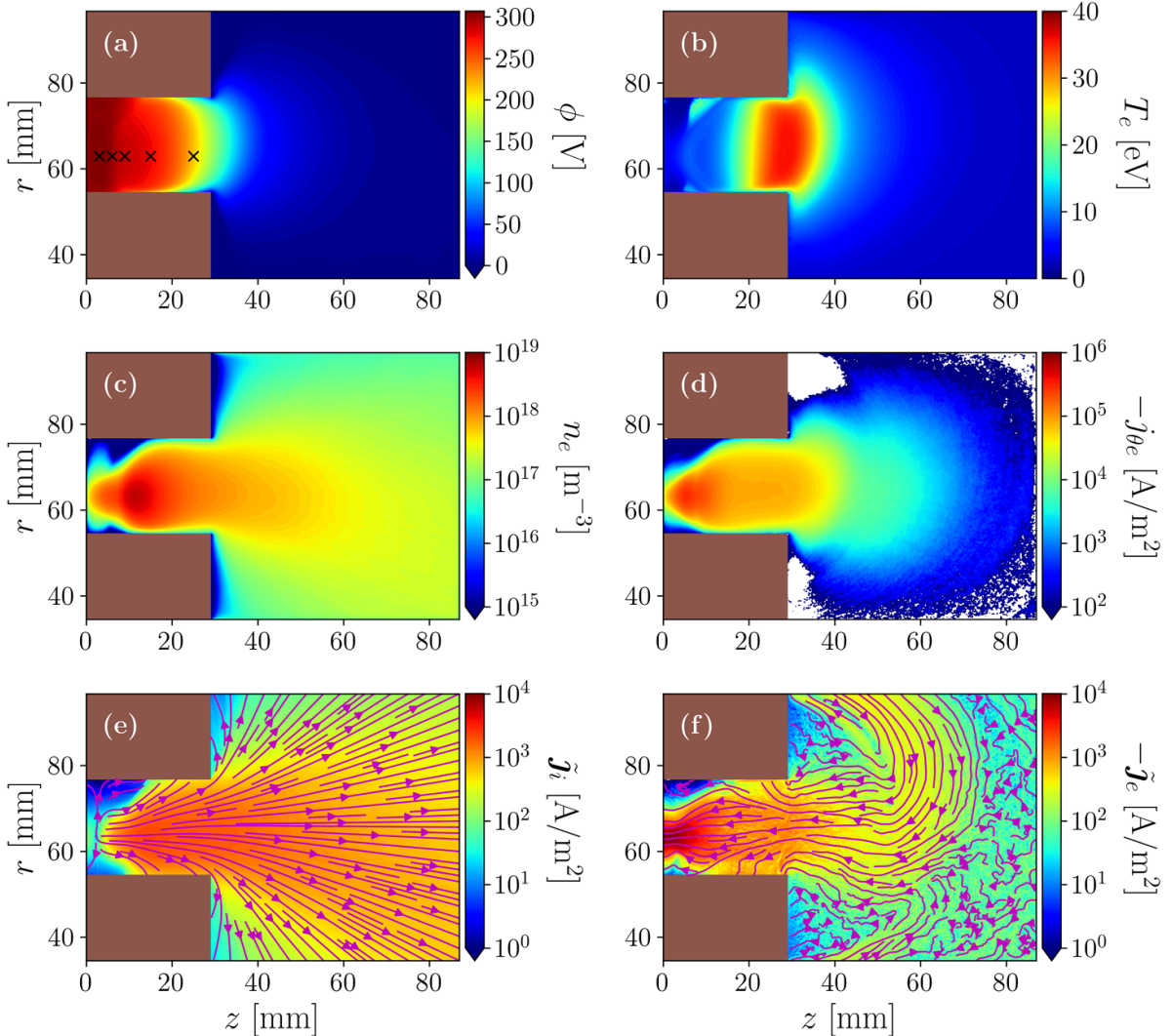


**Figure 3.** Maps of the main macroscopic variables characterizing the discharge at steady-state: (a) electric potential, (b) electron scalar temperature, (c) electron density, (d) azimuthal electron current, (e) and (f) longitudinal ion and electron current densities respectively. Markers in plot (a) indicate the location of the electron and ion VDFs in figures 4 and 5.

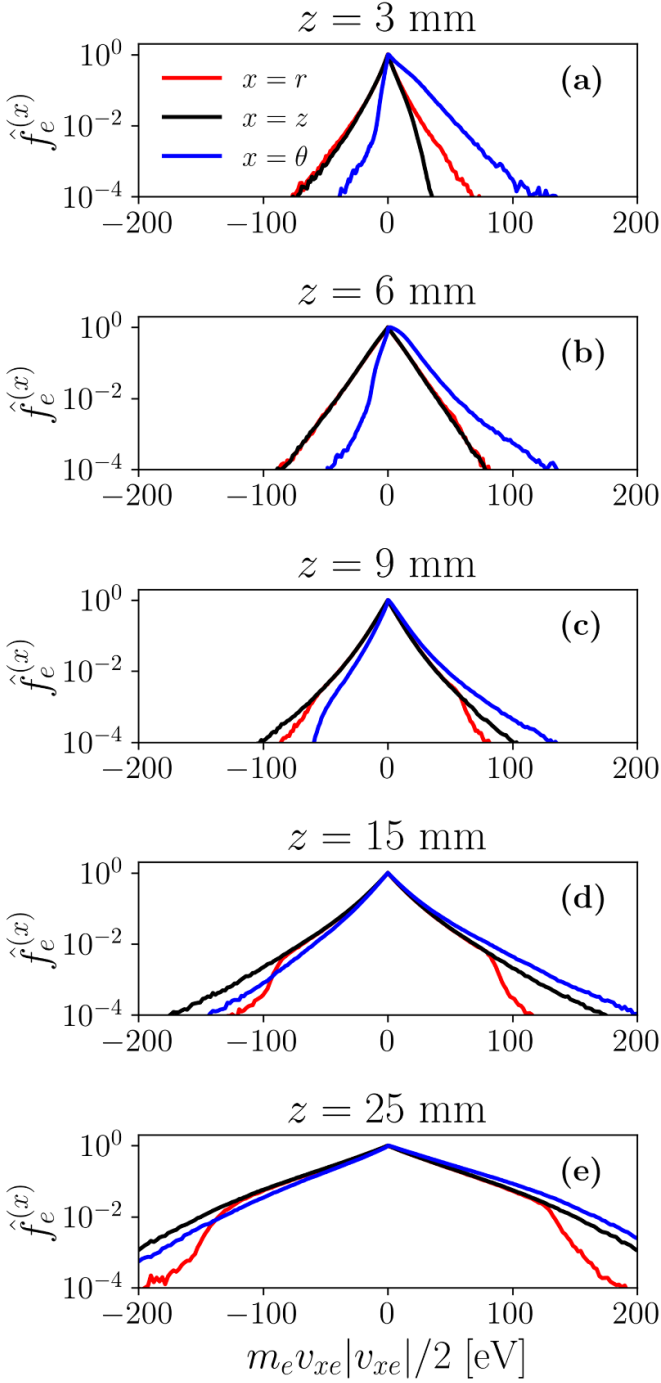
The larger asymmetry between  $\hat{f}_e^{(\theta)}$  and  $\hat{f}_e^{(z)} \simeq \hat{f}_e^{(r)}$  is the signature of  $u_{\theta e}$  approaching  $c_e$ . Close to the anode, at  $z = 3$  mm, an asymmetric  $\hat{f}_e^{(z)}$  can be observed, with more electrons traveling with  $v_z < 0$  than in the opposite direction. This is a consequence of the collection of electrons by the anode wall, as previously observed in [14], which leads to a lower  $T_{ze}$ .

Figure 5 depicts the normalized VDFs of ions. The kinetic response of the nearly unmagnetized and collisionless ions is very different from that of magnetized electrons. Ions are generated via  $e - n$  ionization events and are then accelerated by the electric field. Since ions do not present an  $E \times B$  azimuthal drift and  $E_\theta = 0$  in the axisymmetric approximation, all ions have  $v_\theta \simeq 0$  and  $\hat{f}_i^{(\theta)}(v_\theta)$  resembles a Dirac delta function. Regarding  $\hat{f}_i^{(r)}(v_r)$ , it is near-Maxwellian with a small temperature  $T_{ri}$ . On the contrary, in no place  $\hat{f}_i^{(z)}$  resembles an axially-drifted Maxwellian VDF:  $\hat{f}_i^{(z)}(v_z)$  tends to become monoenergetic near the channel exit, while in the interior we detect the presence of slow new-born ions and

partially accelerated ions. Depending on the relative relevance of these two effects, two-peak VDFs can be found, as observed at  $z = 9$  mm. The large dispersion in ion velocities along  $z$  explains  $T_{zi} > T_{ri}$ . Experimental works measuring the axial ion VDF in HETs using laser-induced fluorescence techniques [38–41] have previously reported dispersion in the axial ion VDF, with the coexistence of slow and fast ions, due to the partial overlap of the ionization and acceleration regions of the thruster discharge.

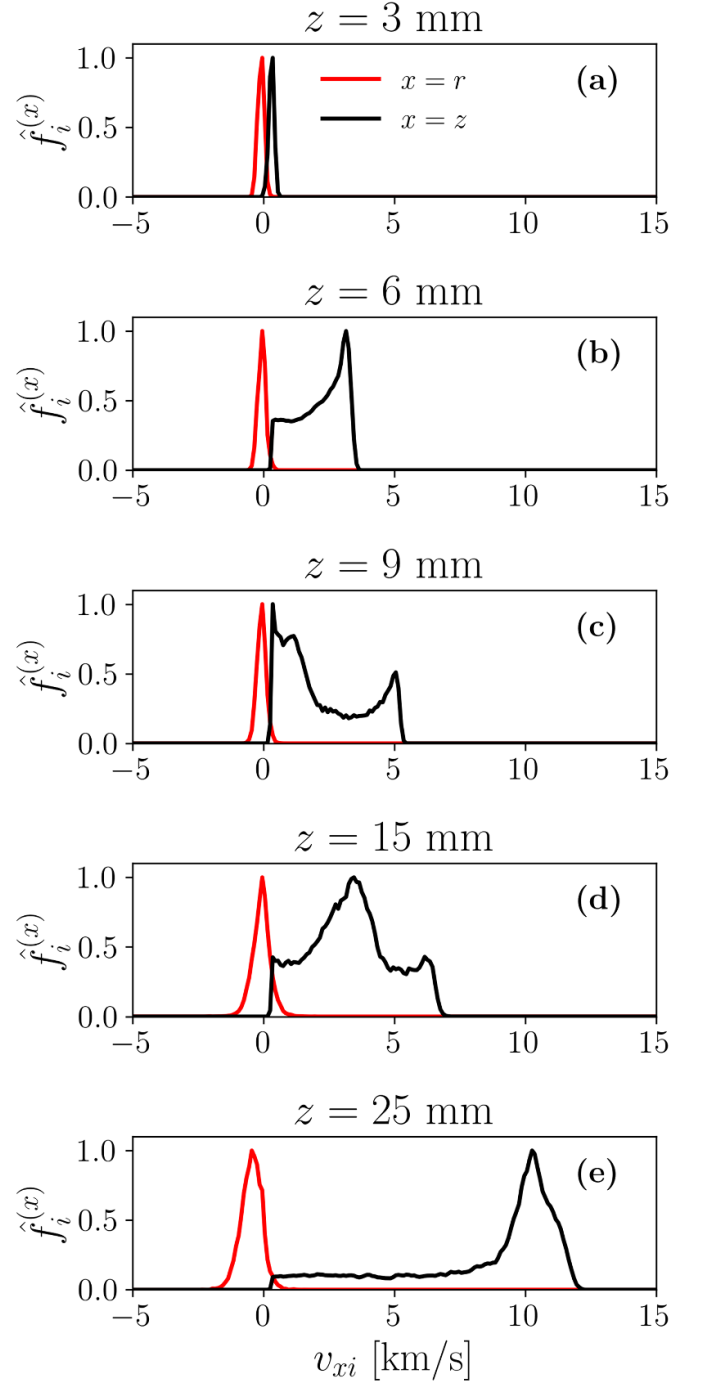
#### 4. Plasma-wall interaction

Figures 6(a) and (b) depict radial profiles of the (normalized) electric potential and plasma density at different axial locations (throughout the paper a single overbar on a variable means a radially-averaged value and subscript M refers to its value at  $r = r_M$ ). Radial profiles near the thruster exit resemble those obtained with a 1Dr PIC model of the discharge with a



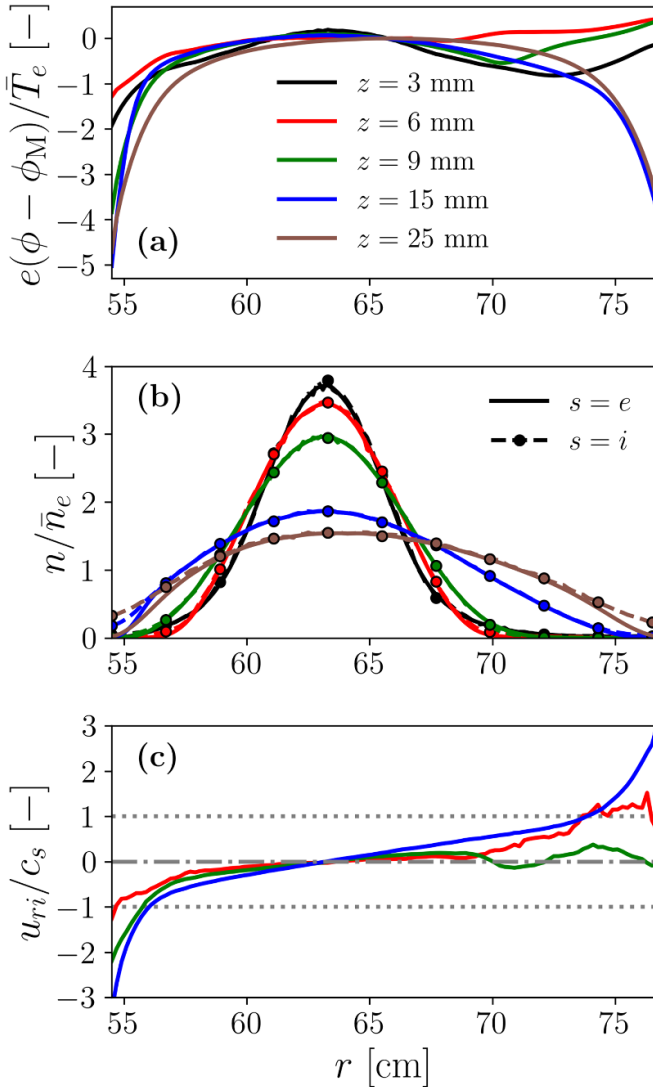
**Figure 4.** Electron 1D axial ( $x = z$ ), radial ( $x = r$ ), and azimuthal ( $x = \theta$ ) VDFs at  $r = r_0$  and different axial locations inside the HET channel, marked in figure 3(a).

purely radial magnetic field [12, 37]. Moving to inner thruster locations,  $n_e$  presents larger radial gradients and reaches lower values near the walls, as found in [19] for a magnetic lens configuration ( $\alpha_B < 0$ ). In all sections, the maximum plasma density is shifted towards  $r \simeq r_0$ . The radial profiles of  $\phi$  at  $z = 25$  and 15 mm present the classical distinction between the quasineutral bulk of plasma and classical (i.e. electron



**Figure 5.** Ion 1D axial ( $x = z$ ) and radial ( $x = r$ ) VDFs at  $r = r_0$  and different axial locations inside the HET channel, marked in figure 3(a).

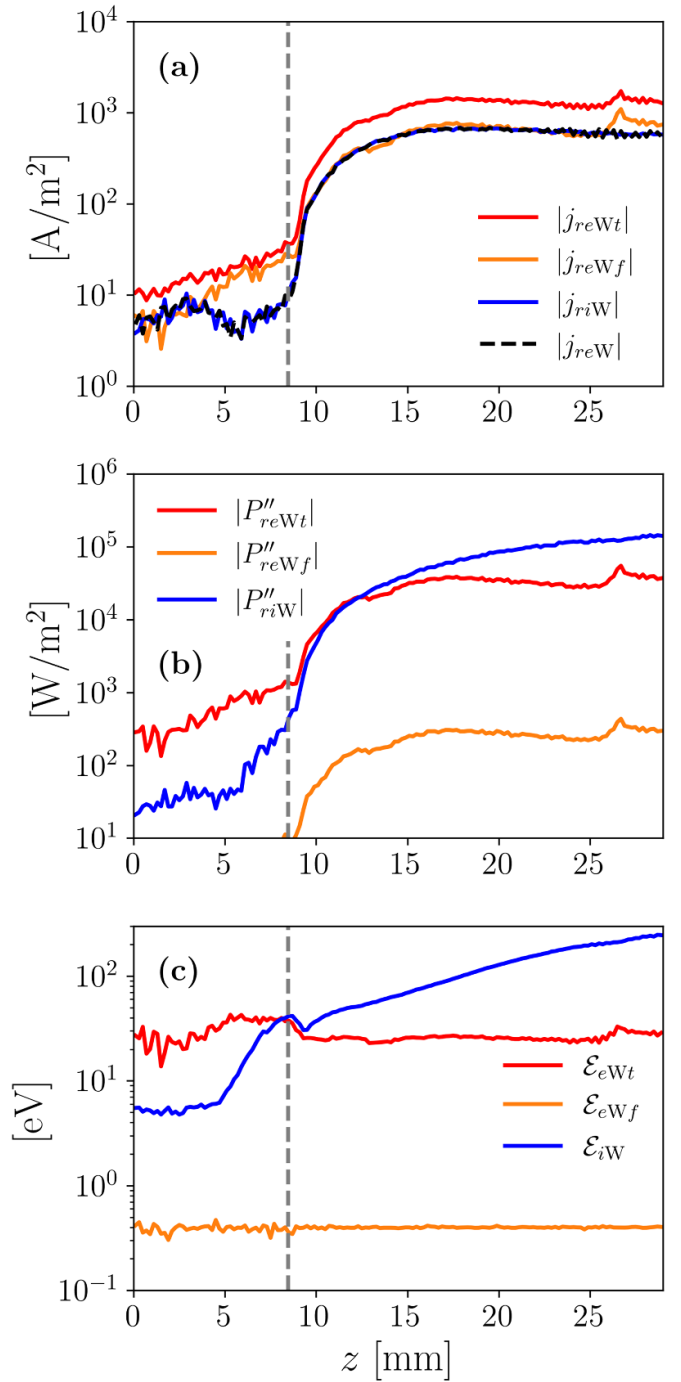
repelling) sheaths, with much larger potential gradients, next to each dielectric wall. This is not the case for the innermost sections, at  $z = 9$ , 6, and 3 mm: the inner wall maintains a sizable sheath at  $z = 9$  mm and a very reduced one at  $z = 6$  and 3 mm. On the contrary, near the outer wall,  $\phi$  grows from the bulk plasma towards the wall with mild  $|\partial\phi/\partial r|$ ; and the classical sheath structure vanishes. The transition between



**Figure 6.** Radial profiles of steady-state macroscopic variables for the reference case simulation at different axial locations: (a) non-dimensional electric potential, (b) non-dimensional ion and electron densities, and (c) non-dimensional ion radial velocity.

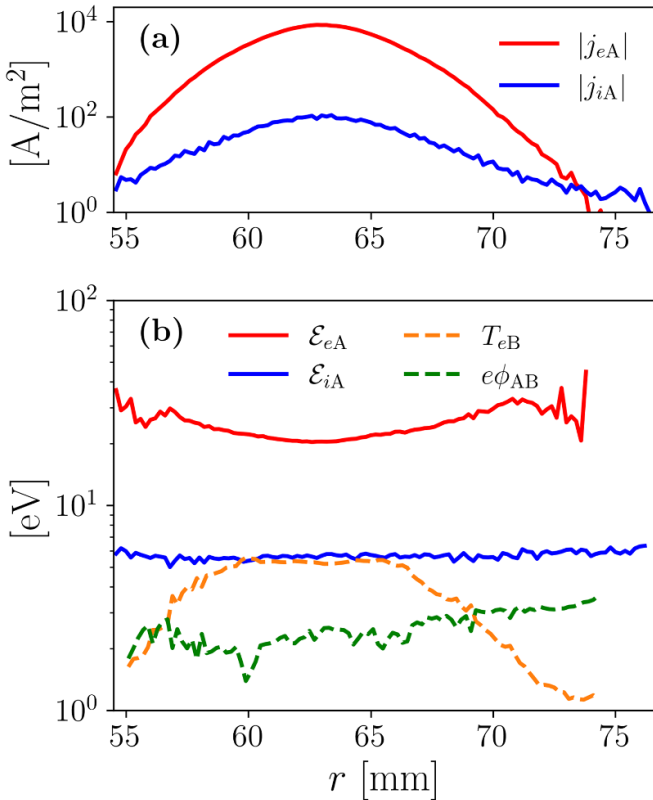
the quasineutral plasma and the Debye sheath is typically considered at the position where the ion velocity normal to the wall becomes sonic (i.e.  $c_s = \sqrt{T_e/m_i}$ ). Figure 6(c) plots the (normalized) radial ion velocity profiles at  $z = 15, 9, 6$  mm, showing an unconventional shape close to the outer wall where the classical sheath structure collapses. The complex plasma behavior in this region will be further analyzed in section 6.

Figure 7 depicts wall interaction magnitudes at the inner wall for electrons and ions. The ion current density to the wall,  $|j_{riW}|$ , the electron current density to the wall,  $|j_{reWt}|$ , and the electron current density emitted from the wall (SEE),  $|j_{rewf}|$  are shown in figure 7(a). At any point, the local zero-current condition is satisfied, i.e.  $|j_{riW}| = |j_{reWt}| - |j_{rewf}| = |j_{rew}|$ . Ion, electron, and SEE energy fluxes,  $|P''_{riW}|$ ,  $|P''_{reWt}|$ , and  $|P''_{rewf}|$ , respectively, are depicted in figure 7(b). Both, current and energy fluxes to the wall, suffer a sharp drop at



**Figure 7.** Wall interaction magnitudes at the inner wall: (a) current densities, (b) energy fluxes, and (c) mean impact/emission energy. The dashed vertical line indicates the location where the MS intersects the inner dielectric wall.

the location where the MS intersects the wall. Similar results are found at the outer wall (not shown). At the inner wall, the average ion current density upstream of the MS is  $6 \text{ A m}^{-2}$ , while downstream it is  $522 \text{ A m}^{-2}$ . At the outer wall, we obtain  $0.2 \text{ A m}^{-2}$  and  $256 \text{ A m}^{-2}$ . Thus, the effect of the MS is stronger at the outer wall and leads to  $|I_{iW1}| > |I_{iW2}|$  (see table 1). Figure 7(c) plots the mean impact energies of ions and



**Figure 8.** Wall interaction magnitudes at the anode: (a) current densities, and (b) mean impact energies for electrons and ions. Plot (b) includes the scalar electron temperature at the ion sonic point B ( $u_{ziB} = -\sqrt{T_{eB}/m_i}$ ) and the potential drop  $e\phi_{AB} = e(\phi_B - \phi_A)$ .

electrons,  $\mathcal{E}_{eW}$  and  $\mathcal{E}_{ewt}$ , respectively, and the mean energy of SEE,  $\mathcal{E}_{ewf}$ . The impact energy of ions,  $\mathcal{E}_{iW} = e|P''_{riW}|/|j_{riW}|$ , varies between  $\sim 30$  eV at  $z = 10$  mm and  $\sim 200$  eV at the channel exit, thus having a big impact on wall erosion there. Conversely, the mean energy of primary electrons, i.e.  $\mathcal{E}_{ewt} = e|P''_{rewt}|/|j_{rewt}|$  is rather uniform along each lateral wall: about 26 eV and 36 eV at the inner and outer walls respectively. Therefore, it deviates from the value of  $2T_e$  (see figure 3(b)) corresponding to Maxwellian electrons. Similar results were obtained in figure 13 of [14] for a purely radial magnetic field, so this feature does not seem to be related to the magnetic curvature. The mean emission energy of SEE agrees with its target value,  $\mathcal{E}_{ewf} = e|P''_{rewf}|/|j_{rewf}| \simeq 0.4$  eV. Since  $\mathcal{E}_{ewf} \ll \mathcal{E}_{ewt}$ , the net electron energy flux,  $|P''_{rew}| = |P''_{rewt}| - |P''_{rewf}|$  corresponds almost entirely to  $|P''_{rewt}|$  even in regions with intense SEE yield.

Figure 8 shows wall interaction magnitudes of ions and electrons at the metallic anode. The particle fluxes are maxima at the location where the separatrix intersects the anode,  $r = r_0$ . A classical electron-repelling Debye sheath is formed at the anode. Assuming that the ion sonic point, where  $u_{zi} = -\sqrt{T_e/m_i}$ , determines the anode sheath edge (B), the scalar electron temperature at B,  $T_{eB}$ ; and the sheath potential drop  $e\phi_{AB} = e(\phi_B - \phi_A)$  are calculated in 8(b). The mild anode sheath ( $\sim 3$  V) justifies the low average ion impact energy at the anode,  $\mathcal{E}_{iA} \simeq 6$  eV in figure 8(b). Electrons reach the anode with a higher energy,  $\mathcal{E}_{eA} \simeq 20$  eV. This result differs from

**Table 1.** Current and power deposited at different surfaces.

Description and symbol	Value and units
Ion current to the anode, $ I_{iA} $	0.29 A
Electron current to the anode, $ I_{eA} $	18.71 A
Ion current to the inner wall, $ I_{iw1} $	3.71 A
Electron current to the inner wall, $ I_{ew1} $	7.75 A
Ion current to the outer wall, $ I_{iw2} $	1.90 A
Electron current to the outer wall, $ I_{ew2} $	6.52 A
Downstream ion beam current, $ I_{iN} $	15.89 A
Discharge power, $I_d V_d$	5527 W
Ion power to the anode, $P_{iA}$	2 W
Electron power to the anode, $P_{eA}$	404 W
Ion power to the inner wall, $P_{iw1}$	498 W
Net electron power to the inner wall, $P_{ew1}$	200 W
Ion power to the outer wall, $P_{iw2}$	264 W
Net Electron power to the outer wall, $P_{ew2}$	234 W
Downstream ion beam power, $P_{iN}$	3568 W

$2T_{eB}$  and is a consequence of the local features of the electron VDF near the anode (not shown), which reveals the presence of two main electron populations. First, there is a low-energy population coming from local ionization. Second, there is a tail of high-energy electrons directed towards the anode. The high-energy tail of the VDF presents a similar slope at different radial locations. This is in line with the relatively high and uniform electron impact energy at the anode wall.

Table 1 gathers the total currents and powers to the different boundaries in steady-state, obtained by integration of local values. Observe that the ion current to the anode is quite small, as desired, and the discharge current is  $I_d = |I_{eA}| - |I_{iA}| \simeq 18.4$ . The inner and outer walls present large asymmetries, as already anticipated. The inner wall, with 70% of the surface of the outer wall, receives almost twice the ion current. This result is consistent with the higher plasma density found in the vicinity of the inner wall in figures 3(c) and 6(b). The secondary electron currents from the lateral walls correspond to SEE effective yields of  $\delta_{s1} \simeq 0.52$  and  $\delta_{s2} \simeq 0.71$  (according with electron impact energies of 26 eV and 36 eV commented above).

## 5. Macroscopic balances

### 5.1. Continuity equation

The radially integrated steady-state current balance for electrons and ions can be expressed as

$$\frac{dI_{zs}}{dz} = \frac{dI_{prod}}{dz} - \frac{dI_{rs}}{dz}, \quad s = i, e, \quad (7)$$

with  $I_{zs}$  the axial current,  $dI_{prod}/dz$  the rate of current production, and  $dI_{rs}/dz$  the rate of current losses to the lateral walls. Figure 9(a) plots the different contributions to this balance. Near the anode, the plasma losses to the walls are very small; therefore, all the plasma production resulting from ionization contributes to the axial current. Conversely, near the thruster

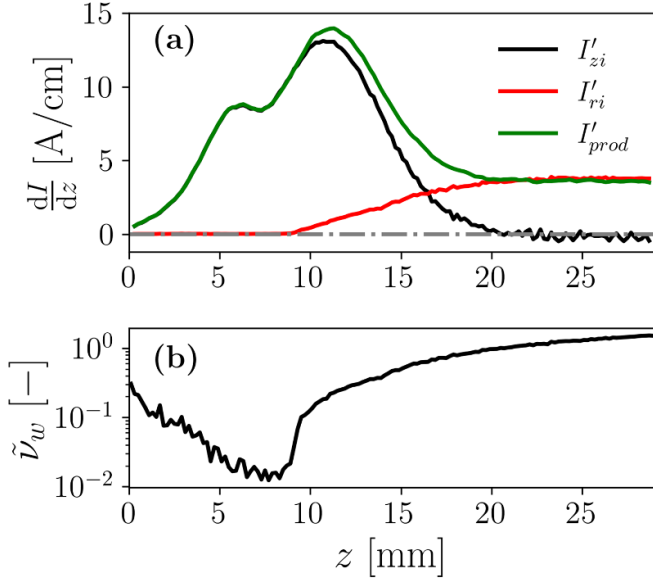


**Figure 9.** Continuity equation: (a) contributions to the current balance (equation (7)) for the ion population (the notation  $' \equiv d/dz$  is used in the legend); (b) non-dimensional wall collisionality parameter defined in [42].

exit, ionization compensates plasma losses to the lateral walls and the axial current is approximately constant.

The 1Dz models of [42–44] describe lateral wall losses as

$$\frac{1}{A} \frac{dI_{rs}}{dz} = e\bar{n}_e \nu_w, \quad \nu_w = \tilde{\nu}_w \frac{2\pi r_M}{A} \sqrt{\frac{T_e}{m_i}} \quad (8)$$

with  $\bar{n}_e$  and  $T_e$  the average plasma density and electron temperature in the cross section respectively, and  $\nu_w$  an equivalent ‘wall-collision frequency’. In the 1Dz model,  $\tilde{\nu}_w$  is a phenomenological parameter to be fitted, which is usually assumed constant; for instance [43, 44] take  $\tilde{\nu}_w = 0.17$  to obtain reasonable lateral losses. Figure 9(b) plots the local  $\tilde{\nu}_w$  for this topology, which is  $\sim 1$  in the near-exit region, and  $\ll 1$  in the near-anode due to the grazing incidence of the magnetic field. It has been checked that with the fully-radial magnetic topology of [14],  $\tilde{\nu}_w \sim 1$  all along the channel.

## 5.2. The electron momentum equation

The radial momentum equation can be expressed as

$$0 \simeq -\frac{\partial p_{rre}}{\partial r} - en_e E_r + j_{\theta e} B_z, \quad (9)$$

since the remaining terms, including inertia, temperature anisotropy, and collisions are found to be negligible in the bulk plasma. Therefore, there is a balance among the pressure, electric, and magnetic forces, the last one due to the curvature of the magnetic field. The different terms of the balance are plotted in figure 10 at several axial sections of the HET channel. Notice first the change of sign of the forces around  $r \approx r_0$

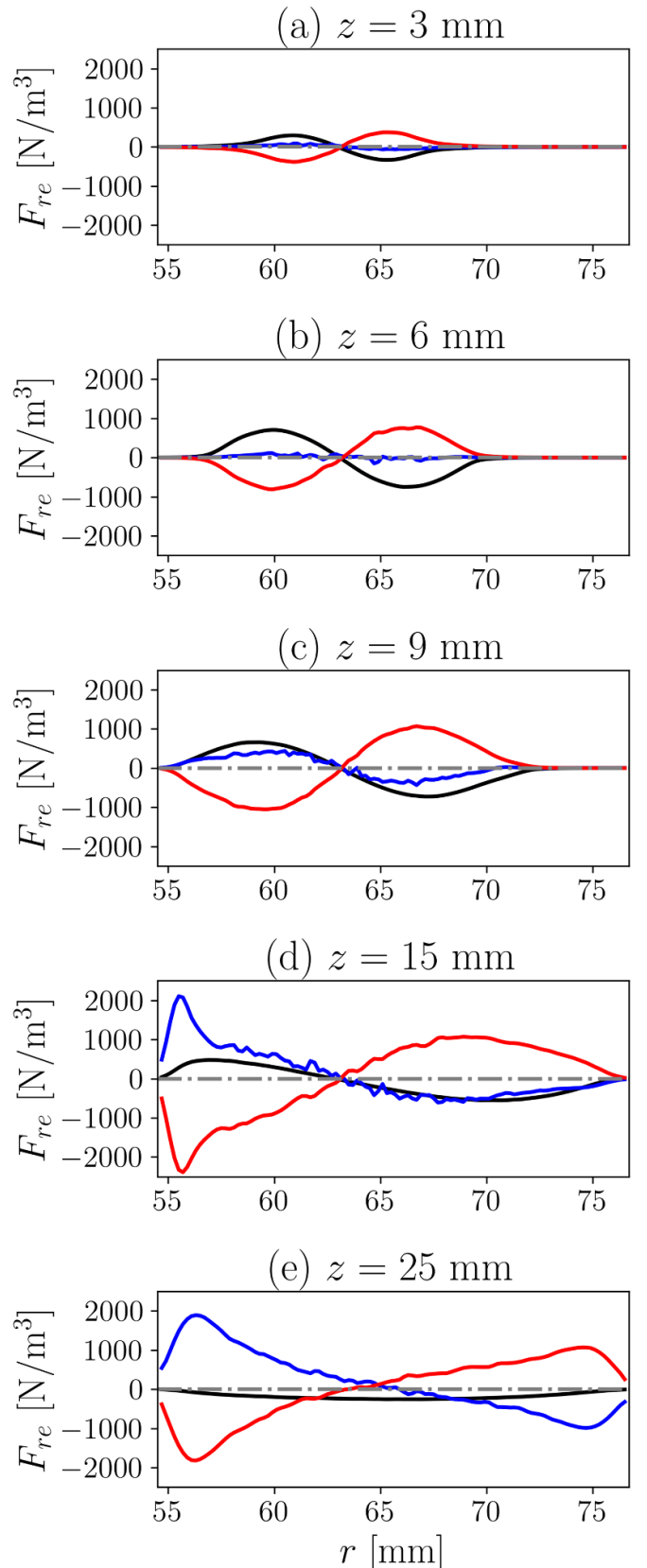


**Figure 10.** Contributions to the radial momentum balance (equation (9)) at five different axial sections. The following radial forces,  $F_{re}$ , are depicted:  $-\partial p_{rre}/\partial r$  (red),  $-en_e E_r$  (blue),  $j_{\theta e} B_z$  (black).

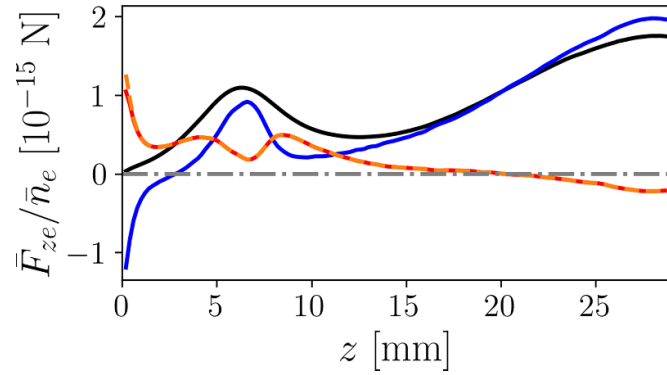


**Figure 11.** Contributions to the (radially averaged) axial electron momentum balance (equation (10)). The following axial forces,  $F_{ze}$ , are depicted:  $-j_{\theta e}B_r$  (—),  $en_eE_z$  (—),  $\partial M_{zze}/\partial z$  (—), and  $\partial p_{zze}/\partial z$  (---).

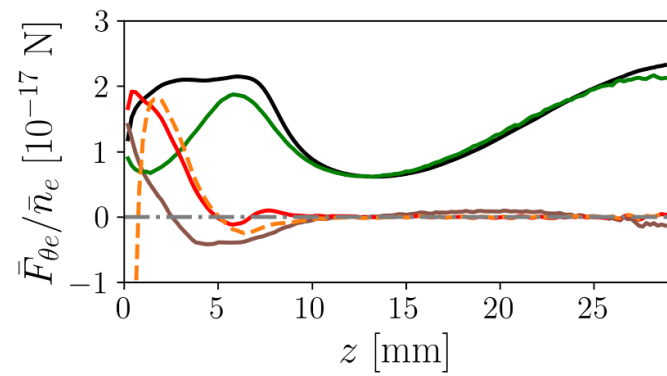


**Figure 12.** Contributions to the (radially averaged) azimuthal electron momentum balance (equation (11)). The following azimuthal forces,  $F_{\theta e}$ , are depicted:  $j_{ze}B_r$  (—),  $-j_{re}B_z$  (—),  $-F_{col,\theta e}$  (—),  $\partial M_{z\theta e}/\partial z$  (—), and  $\partial p_{z\theta e}/\partial z$  (---).

(except at  $z = 25$  mm for the magnetic force, which anyway is rather small). Except for this anomaly, we observe that at both sides of  $r \approx r_0$ , the pressure force has an expanding character (i.e. pushing electrons towards the two lateral walls), while the electric and magnetic forces have a confining character; of these two, the magnetic force dominates near the anode and the electric force near the thruster exit.

The axial momentum equation can be approximated by the classical expression

$$0 \simeq -\frac{\partial p_{zze}}{\partial z} - en_eE_z - j_{\theta e}B_r, \quad (10)$$

stating that the azimuthal drift combines  $E \times B$  and diamagnetic drifts. Collisional and  $\partial M_{rze}/\partial z$  contributions are subdominant with respect to the strong axial electron pressure gradient and electric force. Figure 11 plots this axial balance for radially-averaged variables, and shows also that axial electron inertia effects (i.e.  $m_e n_e u_{ze}^2 = M_{zze} - p_{zze}$ ) are negligible. In fact, the plasma response close to the anode resembles that of an unmagnetized plasma, in which the pressure and electric force balance, and the magnetic force becomes small. The complex behavior in the near-anode region is responsible for the local extrema of the profiles at  $z \sim 7$  mm.

Finally, the azimuthal electron momentum equation reads

$$0 \simeq -\frac{\partial M_{z\theta e}}{\partial z} + j_{ze}B_r - j_{re}B_z + F_{col,\theta e}. \quad (11)$$

The term  $\partial M_{z\theta e}/\partial z$ , combining inertia and gyroviscous contributions, is a kinetic finite-Larmor-radius (FLR) effect [45, 46]. Figure 12 compares the radially averaged terms in equation (11). Observe first that the dominant terms are much smaller (typically 2 orders of magnitude) than in the axial momentum balance in equation (10). Near the thruster exit both  $j_{ze}B_r$  and  $\partial M_{z\theta e}/\partial z$  are small, and the classical result  $j_{ze}B_r \simeq -F_{col,\theta e}$  is retrieved. Conversely, near the anode, all the terms in equation (11) become relevant. The relevance of FLR effects, particularly near the anode, is found in other 1Dz [13] and 2Dzθ [47] kinetic studies and also in our previous work [14] where  $\mathbf{B}$  was purely radial. Finally, observe that equation (11) determines  $j_{\perp e} = (j_{ze}B_r - j_{re}B_z)/B$ , i.e. the current density perpendicular to  $\mathbf{B}$  (or cross-field current). This equation must be completed with the 2D electron continuity equation to determine  $j_{ze}$  and  $j_{re}$  individually. Only where  $B_z$  is negligible, the cross-field current is the axial current, the one that defines the electron current collected by the anode.

### 5.3. The electron energy flux vector

The stationary electron energy equation is

$$\nabla \cdot \mathbf{P}_e'' = \mathbf{j}_e \cdot \mathbf{E} - P_{\text{inel}}''' \quad (12)$$

where  $\mathbf{P}_e''$  is the electron energy flux vector,  $\mathbf{j}_e \cdot \mathbf{E}$  the work of the electric field and  $P_{\text{inel}}'''$  the power spent in

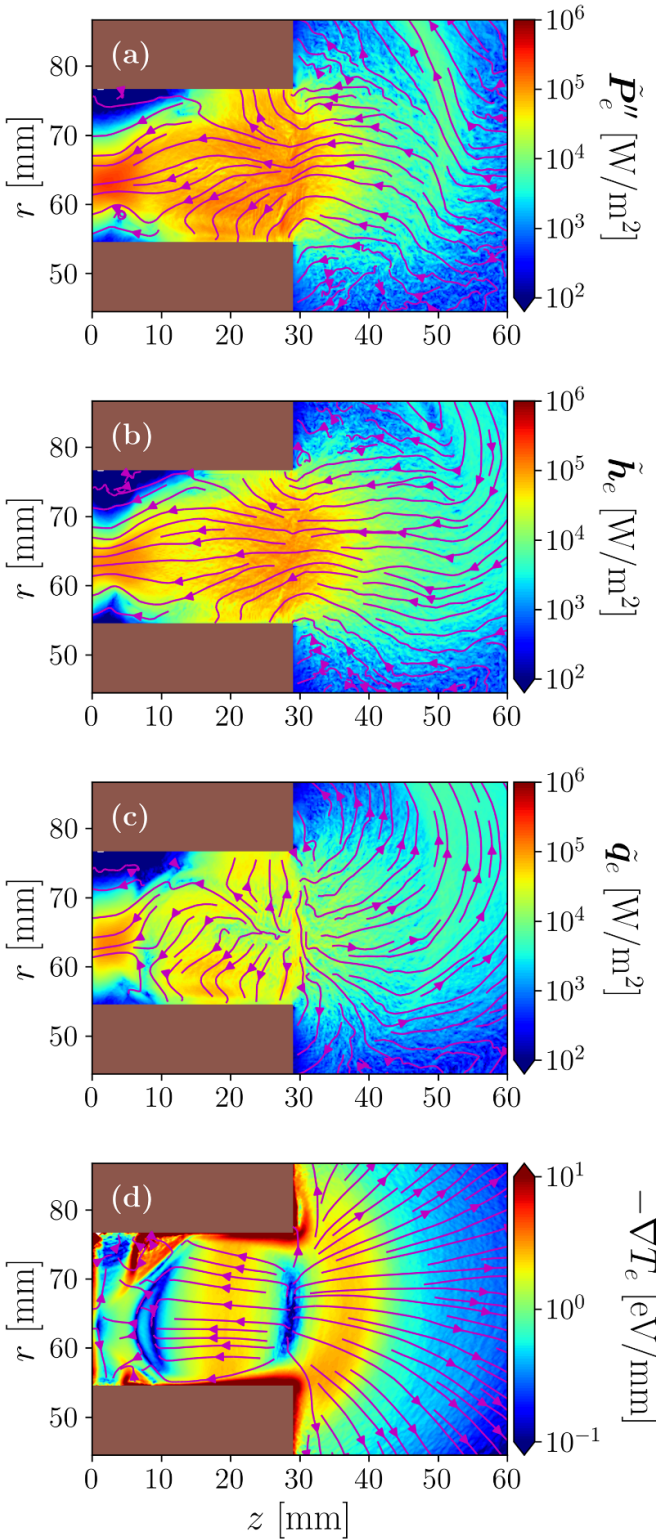


**Figure 13.** The electron energy flux vector: (a) total electron energy flux vector, (b) enthalpy flux vector, (c) heat flux vector, and (d) electron temperature gradient.

inelastic collisions. In a macroscopic formulation, the energy flux is commonly expressed as the sum of four different contributions:

$$\mathbf{P}_e'' = \mathbf{h}_e + \mathbf{q}_e + \mathbf{U}_e + \Pi_e, \quad (13)$$

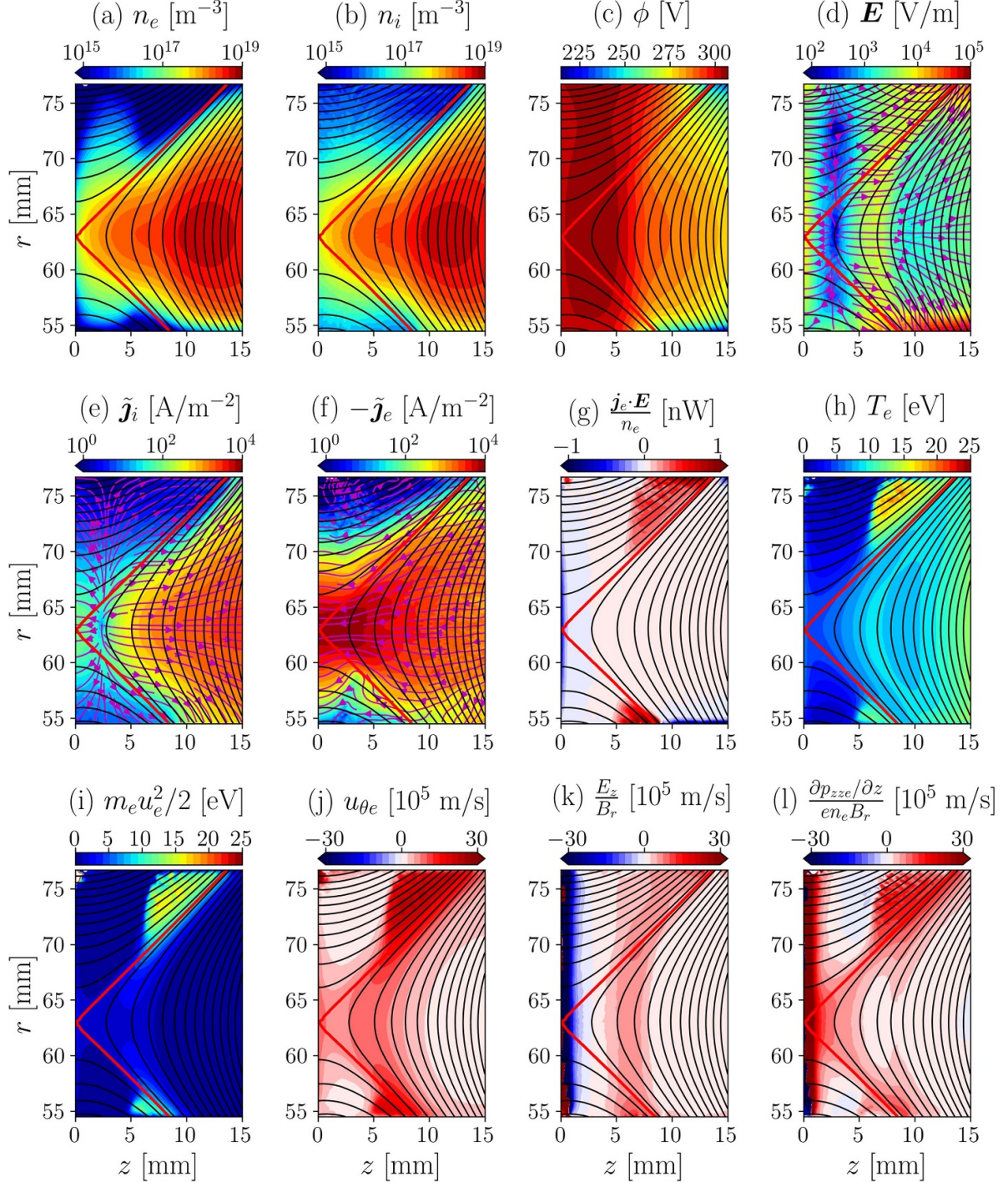
with  $\mathbf{h}_e = (5/2)n_e T_e \mathbf{u}_e$  the enthalpy flux,  $\mathbf{q}_e$  the heat flux,  $\mathbf{U}_e = m_e u_e^2 n_e \mathbf{u}_e / 2$  the flux of kinetic energy of the fluid flow and  $\Pi_e = (\bar{p}_e - p_e \bar{I}) \cdot \mathbf{u}_e$  the energy flux coming from anisotropic and non-gyrotropic features of the pressure tensor.

Figure 13(a) plots the longitudinal electron energy flux vector,  $\mathbf{P}_e''$ , computed from the PIC results. The analysis of the different terms in equation (13) reveals that contributions from both  $\mathbf{U}_e$  and  $\Pi_e$  are negligible except near the MS due to large electron inertia. Thus, they are omitted in figure 13. The main contributors to the electron energy flux vector are shown in figures 13(b) and (c). The enthalpy flux vector constitutes the dominant contribution to  $\mathbf{P}_e''$  inside the thruster. The sub-dominant contribution comes from  $\tilde{\mathbf{q}}_e$ , which axially points towards the anode as  $\mathbf{h}_e$ . In the near plume  $\tilde{\mathbf{h}}_e$  and  $\tilde{\mathbf{q}}_e$  compete and tend to point in different directions. At the thruster exit, where  $T_e$  reaches its maximum value,  $\tilde{\mathbf{q}}_e$  changes sign. This suggests a dependence with  $\nabla T_e$  and thus a classical conductive response. In an attempt to establish a correlation,  $\nabla T_e$  is computed in figure 13(d). However, the behavior of  $\tilde{\mathbf{q}}_e$  is too complex to be amenable to a simple law, and hence the same happens with  $\tilde{\mathbf{P}}_e''$ .

## 6. Analysis of the near-anode region

In order to analyze the complex plasma response near the anode, figure 14 zooms in the region that extends from the anode to  $z = 15$  mm. The magnetic field has a strong influence on the plasma behavior, and the MS acts as a boundary between the different regions. As shown in figure 1, downstream of the MS, the magnetic field presents a conventional magnetic lens topology; while upstream of the MS, the magnetic field features a large curvature and partially shields the lateral dielectric walls.

Figure 14(f) plots the longitudinal electron current density with streamlines. It shows that once the electron flow reaches the MS it follows the most electrically favorable path (i.e. along the MS) and reaches the anode around the near-null point. This prevents most of the magnetized electrons from reaching the region upstream of the MS. Consequently, the electron density presents a sharp jump across the MS, as shown in figure 14(a). This effect is stronger near the outer wall because it is farther away from the null point, and thus  $\mathbf{B}$  is stronger there. The lateral walls of the thruster are dielectric, and therefore, at steady-state, they cannot collect net electric current from the plasma, i.e.  $|j_{rw}| = |j_{iw}|$ . Since the electron current to the wall is so small in this region, very few ions must reach the wall. The current of unmagnetized ions, in figure 14(e), is controlled by the combined action of ion production and the electric field. The electric potential  $\phi$  and its gradient  $\mathbf{E}$  self-adjust to achieve the appropriate response of electrons and ions. The most unconventional feature is that the electric potential grows from the plasma to the outer dielectric wall, as already anticipated in figure 6(a). This is contrary to the case of a classical electron-repelling sheath and leads to local electric field reversal (i.e. electron attracting and ion repelling), as shown in figure 14(d). The ion density, in figure 14(b), tries to follow the electron density to keep the



**Figure 14.** Macroscopic plasma variables near the anode: (a) electron density, (b) ion density, (c) electric potential, (d) electric field, (e) longitudinal ion current density, (f) longitudinal electron current density, (g) power of the electric field on the electron population per unit particle, (h) scalar electron temperature, (i) kinetic energy of the electron fluid flow, (j) azimuthal electron velocity, (k) and (l) depict the main contributions to  $u_{\theta e}$  from equation (10). Black contours represent magnetic field lines and the MS is plotted in red.

plasma quasineutral, but this fails in the triangles around the anode corners, where  $n_i > n_e$ .

Moving into electron energy considerations, the electric field work is the main source of energy for electrons (see equation (12)). Figure 14(g) shows the 2D map of power deposited by the electric field per electron particle,  $j_e \cdot E / n_e$ . It presents very high relative values near the lateral walls,

immediately upstream of the MS. These are due to a relatively mild change in both  $j_e$  and  $E$  and the strong decrease in  $n_e$ . The consequence is a large increase of both, the electron thermal energy (see  $T_e$  in figure 14(h)), and the kinetic energy of the fluid flow (see  $m_e u_e^2 / 2$  in figure 14(i)). Indeed,  $m_e u_e^2 / 2 \sim T_e$  in this region, breaking the drift-diffusive approximation there. The fluid electron velocity dominated by

$u_{\theta e}$ , suffers a steep change across the MS (see figure 14(j)). The local analysis of the different terms in the axial momentum equation (equation (10), in figures 14(k) and (l)) reveals that the increase of  $u_{\theta e}$  is mainly driven by the term  $\partial p_{zze} / \partial z$ ; which becomes large due to the sharp change in  $n_e$  across the MS (in figure 14(a)).

## 7. Conclusions

A 2D-3 V axisymmetric PIC model has been used to discuss the effect of magnetic curvature on the kinetic plasma response in a HET, focusing mainly on the electron population behavior. The simulation code of [14] was applied to simulate a 5 kW class Hall thruster similar to the PPS5000.

Consistently with our previous study for purely radial magnetic topology [14] we find: (1) the mean electron energy to the walls does not correspond to  $2T_e$ ; (2) the electron energy flux is mainly given by the enthalpy and the heat flux, the latter not following a simple Fourier law; (3) FLR effects play an important role in the azimuthal electron momentum equation in the near anode region. Near the thruster exit, where the magnetic field is approximately radial, the high-energy tail of the radial electron VDF is largely depleted, as in [37]. In the central region, with a moderately curved magnetic field, there is a higher replenishment of the VDF tails, in agreement with [19].

However, in the two ‘triangular’ regions bounded by the MS and the anode, the response is unconventional. Upstream of the MS, the magnetic field partially shields the lateral walls of the channel and confines the electrons away from them. The plasma density is maximum around  $r_0$ , the radial location of the near-null magnetic point at the anode wall, and decreases towards the lateral walls by two or three orders of magnitude. This implies a similar reduction in the electron current and energy fluxes to the walls. To comply with the local dielectric condition at the walls, the classical sheath structure collapses, and, instead, the electric potential grows from the bulk plasma to the wall attracting electrons and repelling unmagnetized ions. The power of the electric field on electrons in this region increases both, the thermal energy and the kinetic energy of the fluid flow. The latter becomes comparable to the former, invalidating the drift-diffusive approximation. The numerical simulation shows that the plasma fluxes to the walls are effectively reduced upstream of the separatrix for this magnetic configuration. However, although locally it seems to be beneficial, it is difficult to determine if it would improve the overall thruster performance.

The near-anode is a region of very difficult access for diagnostics, and few experimental works have characterized the plasma there. Therefore, experimental verification of the numerical results presented here is lacking. In the simulation, the unconventional plasma response upstream of the MS is a consequence of the low cross-field electron mobility. Therefore, a self-consistent characterization of this region requires a 3D kinetic description of the plasma discharge, that takes into account azimuthal instabilities, wall collection, and axial plasma transport effects. Sheath reversal due to grazing magnetic incidence could also be present in magnetic

shielding topologies, where the magnetic field is almost parallel to the walls. The analysis of such topologies will be addressed in a future publication.

## Data availability statement

The data cannot be made publicly available upon publication because they are not available in a format that is sufficiently accessible or reusable by other researchers. The data that support the findings of this study are available upon reasonable request from the authors.

## Acknowledgments

This work has been supported by the R&D project HEEP (PID2022-140035OB-I00) funded by MCIN/AEI/10.13039/501100011033 and by ‘ERDF A way of making Europe’. The authors thank E. Bello-Benítez for his contribution to the development of code.

## Appendix. Effect of numerical parameters in the plasma solution

Additional simulations have been performed to verify the robustness of the numerical results. The effect of the domain size and time-step were addressed in [31]. The simulated domain is large enough so that the results in the thruster channel are insensitive to the plume size. Moreover, results do not change if a smaller  $\Delta t$  is used. Here, we address the effect of the number of simulated particles,  $N_p$ , and the augmentation factor for the vacuum permittivity,  $f_D$ . For the different numerical experiments, axial profiles of macroscopic magnitudes at  $r_M$  and local electron current densities to different thruster surfaces are provided in figure 15. Maps of macroscopic magnitudes near the anode are shown in figure 16.

First, simulations that double and quadruple the number of simulated particles,  $N_p$ , keeping identical meshes, time-step, and  $f_D$ , match reasonably well the results of the reference simulation. The small quantitative changes are an indication that  $N_p$  does not significantly affect the solution, and the results of the reference case are robust.

Second, we address the effect of the augmented vacuum permittivity. In [14], we found that simulations with  $f_D = 5$  and 10 were almost indistinguishable, while a simulation with  $f_D = 20$  presented larger deviations. In order to prove that the simulation results are not affected by our choice of  $f_D = 12$ , an additional test case, with  $f_D = 8$ , was simulated. The mesh size was reduced ( $\Delta z = \Delta r = 100 \mu\text{m}$ ) and, consequently, the time-step was adjusted ( $\Delta t = 10 \text{ ps}$ ). The number of particles per cell was set to be the same as in the reference case. The solutions in both cases are nearly identical, showing that the augmented Debye length has a weak effect on the simulation results within this range of  $f_D$ .

Inevitably, numerical thermalization is present in PIC simulations [48]. In order to minimize its effects on the simulation results, it has to occur in time scales that are longer than other relevant phenomena affecting the electron

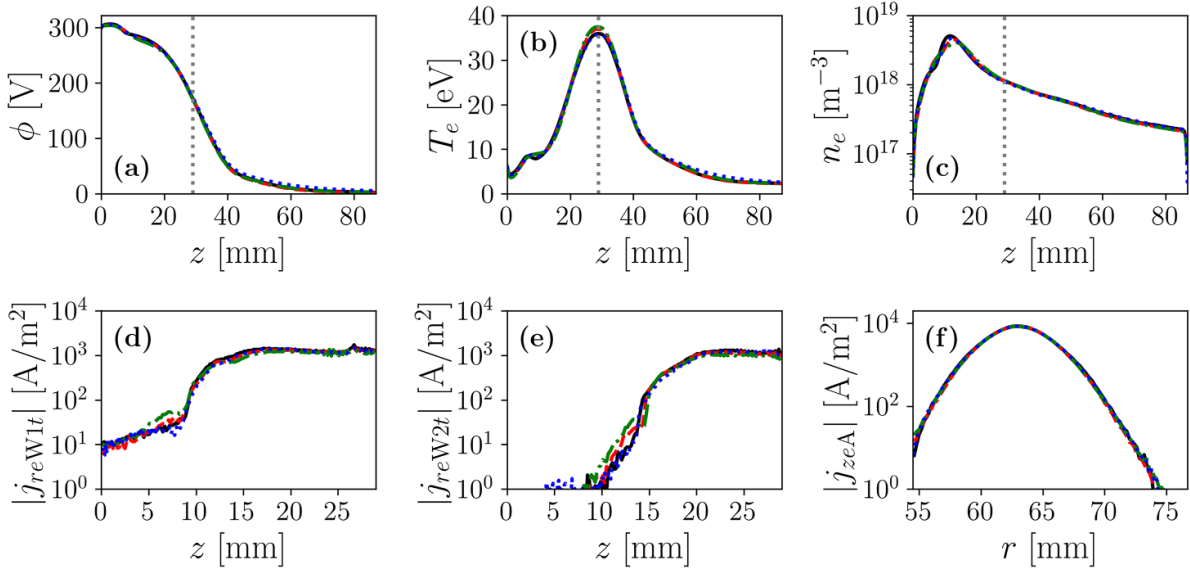


**Figure 15.** Comparison of simulations with different numerical parameters (Reference (—),  $2N_p$  (---),  $4N_p$  (-·-), and  $f_D = 8$  (.....)). First row, axial profiles at  $r_M$ : (a) electric potential, (b) scalar electron temperature, and (c) electron density. Second row, electron current densities to different thruster surfaces: (d) inner wall, (e) outer wall, and (f) anode.

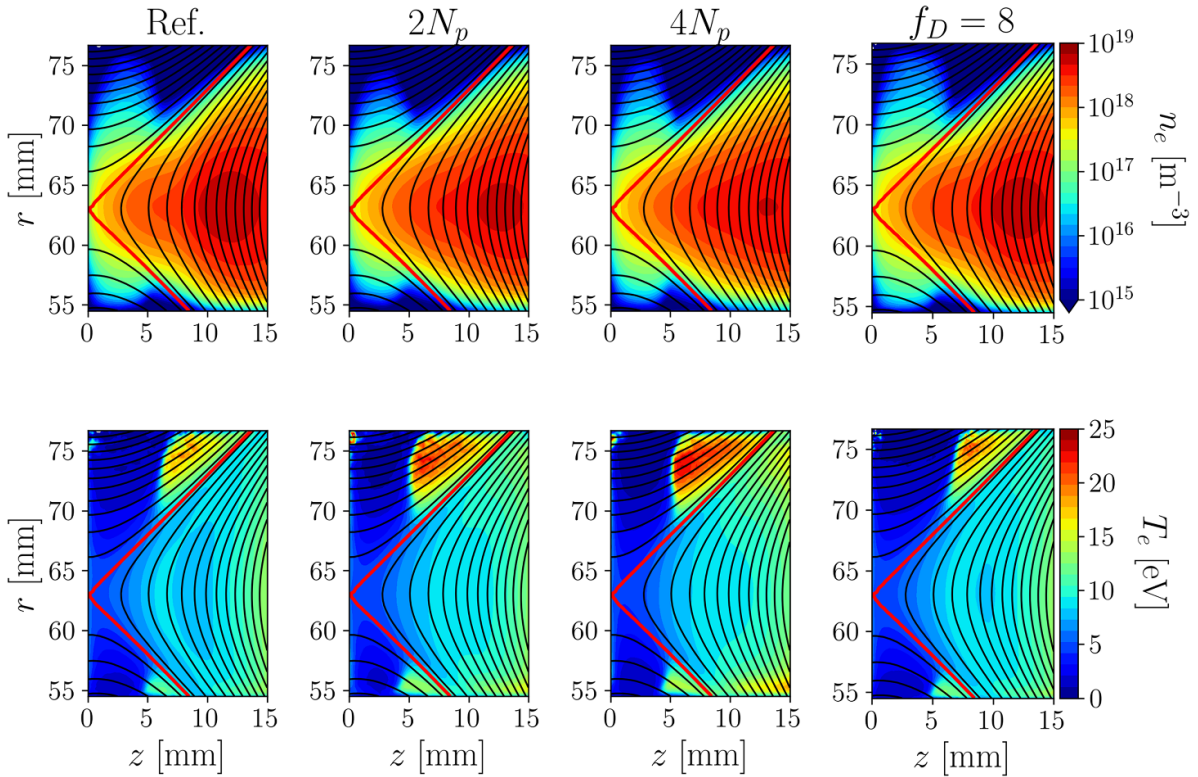


**Figure 16.** Comparison of the electron density (first row) and temperature (second row) near the anode for simulations with different numerical parameters: Reference (first column),  $2N_p$  (second column),  $4N_p$  (third column), and  $f_D = 8$  (fourth column).

VDF. Considering  $f_D = 12$  and typical values for  $n_e = 3 \cdot 10^{18} \text{ m}^{-3}$  and  $T_e = 20 \text{ eV}$ , the number of macroparticles per Debye volume is  $N_D \simeq 100$ , yielding a numerical thermalization equivalent frequency of  $7.22 \cdot 10^6 \text{ s}^{-1}$ . A characteristic value for the anomalous collision frequency is  $5.29 \cdot 10^7 \text{ s}^{-1}$  and the inverse of the radial transit time of an electron

is estimated as  $\bar{c}_e/(r_{W2} - r_{W1}) \simeq 1.35 \cdot 10^8 \text{ s}^{-1}$ . Therefore, other phenomena dominate over numerical thermalization. This is further confirmed by the weak variation in the results shown in cases with a larger number of simulated particles, for which a lower numerical thermalization is expected.

## ORCID iDs

A Marín-Cebrián  0000-0001-6702-2819  
 E Ahedo  0000-0003-2148-4553  
 A Domínguez-Vázquez  0000-0003-3935-7333

## References

- [1] Kaganovich I D *et al* 2020 Perspectives on physics of ExB discharges relevant to plasma propulsion and similar technologies *Phys. Plasmas* **27** 120–601
- [2] Fife J M 1998 Hybrid-PIC modeling and electrostatic probe survey of Hall thrusters *PhD Thesis* Massachusetts Institute of Technology
- [3] Sommier E, Scharfe M K, Gascon N, Cappelli M A and Fernandez E 2007 Simulating plasma-induced Hall thruster wall erosion with a two-dimensional hybrid model *IEEE Trans. Plasma Sci.* **35** 1379–87
- [4] Ortega A L, Mikellides I G, Sekerak M J and Jorns B A 2019 Plasma simulations in 2-D (rz) geometry for the assessment of pole erosion in a magnetically shielded Hall thruster *J. Appl. Phys.* **125** 033302
- [5] Perales-Díaz J, Domínguez-Vázquez A, Fajardo P, Ahedo E, Faraji F, Reza M and Andreussi T 2022 Hybrid plasma simulations of a magnetically shielded Hall thruster *J. Appl. Phys.* **131** 103302
- [6] Bittencourt J A 2004 *Fundamentals of Plasma Physics* (Springer)
- [7] Ahedo E 2023 Using electron fluid models to analyze plasma thruster discharges *J. Electr. Propuls.* **2** 2
- [8] Taccogna F, Cichocki F, Eremin D, Fubiani G and Garrigues L 2023 Plasma propulsion modeling with particle-based algorithms *J. Appl. Phys.* **134** 150901
- [9] Taccogna F, Longo S and Capitelli M 2005 Plasma sheaths in Hall discharge *Phys. Plasmas* **12** 093506
- [10] Kaganovich I D, Raitses Y, Sydorenko D and Smolyakov A 2007 Kinetic effects in a Hall thruster discharge *Phys. Plasmas* **14** 057104
- [11] Taccogna F, Schneider R, Longo S and Capitelli M 2008 Kinetic simulations of a plasma thruster *Plasma Sources Sci. Technol.* **17** 024003
- [12] Domínguez-Vázquez A, Taccogna F and Ahedo E 2018 Particle modeling of radial electron dynamics in a controlled discharge of a Hall thruster *Plasma Sources Sci. Technol.* **27** 064006
- [13] Yamashita Y, Lau R and Hara K 2023 Inertial and anisotropic pressure effects on cross-field electron transport in low-temperature magnetized plasmas *J. Phys. D: Appl. Phys.* **56** 384003
- [14] Marín-Cebrián A, Bello-Benítez E, Domínguez-Vázquez A and Ahedo E 2024 Non-Maxwellian electron effects on the macroscopic response of a Hall thruster discharge from an axial–radial kinetic model *Plasma Sources Sci. Technol.* **33** 025008
- [15] Kim V 1998 Main physical features and processes determining the performance of stationary plasma thrusters *J. Propulsion Power* **14** 736–43
- [16] Belikov M B, Gorshkov O A, Rizakhanov R N, Shagayda A A and Khartov S A 1999 Hall-type low- and mean-power thrusters output parameters *35th Joint Propulsion Conf. (Los Angeles, CA)* p AIAA-99-2571
- [17] Morozov A I and Savel'yev V V 2000 Fundamentals of Stationary Plasma Thruster Theory *Reviews of Plasma Physics* vol 21 (Kluwer Academic)
- [18] Miedzik J, Barral S and Daničko D 2015 Influence of oblique magnetic field on electron cross-field transport in a Hall effect thruster *Phys. Plasmas* **22** 043511
- [19] Marín-Cebrián A, Domínguez-Vázquez A, Fajardo P and Ahedo E 2022 Kinetic plasma dynamics in a radial model of a Hall thruster with a curved magnetic field *Plasma Sources Sci. Technol.* **31** 115003
- [20] Cho S, Komurasaki K and Arakawa Y 2013 Kinetic particle simulation of discharge and wall erosion of a Hall thruster *Phys. Plasmas* **20** 063501
- [21] Szabo J, Warner N, Martinez-Sánchez M and Batischhev O 2014 Full particle-in-cell simulation methodology for axisymmetric Hall effect thrusters *J. Propuls. Power* **30** 197–208
- [22] Liu J, Hong Li, Yanlin H, Liu X, Ding Y, Wei L, Daren Y and Wang X 2019 Particle-in-cell simulation of the effect of curved magnetic field on wall bombardment and erosion in a Hall thruster *Contrib. Plasma Phys.* **59** e201800001
- [23] Dong M, Zeng D, Wang L, Ding Y, Wei L, Hong Li and Daren Y 2020 Numerical simulation study on the influence of channel geometry on discharge characteristics of low-power magnetically shielded Hall thrusters *Vacuum* **180** 109547
- [24] Taccogna F, Cichocki F and Minelli P 2022 Coupling plasma physics and chemistry in PIC model of electric propulsion: application to an air-breathing low power Hall thruster *Frontiers* **10** 1006994
- [25] Cho S, Watanabe H, Kubota K, Iihara S, Fuchigami K, Uematsu K and Funaki I 2015 Study of electron transport in a Hall thruster by axial–radial fully kinetic particle simulation *Phys. Plasmas* **22** 103523
- [26] Duchemin O, Rabin J, Balika L, Coduti G, Vial V, Vuglec D, Cavelan X and Leroi V 2019 Qualification status of the PPS-5000 Hall thruster unit *36th Int. Electric Propulsion Conf. (IEPC-2019-906)* (Electric Rocket Propulsion Society)
- [27] Duchemin O B, Rabin J, Coduti G and Méhauté D L 2023 Expanding the mission capture of the PPS® 5000 Hall thruster *ASCEND 2023* p 4790
- [28] Garrigues L, Hagelaar G J M, Bareilles J, Boniface C and Boeuf J P 2003 Model study of the influence of the magnetic field configuration on the performance and lifetime of a Hall thruster *Phys. Plasmas* **10** 4886
- [29] Mazouffre S, Bourgeois G, Vaudolon J, Garrigues L, Hénaux C, Dominique Harribey R V, Rossi A, Zurbach S and Méhauté D L 2015 Development and testing of Hall thruster with flexible magnetic field configuration *J. Propuls. Power* **31** 1167–74
- [30] Andreussi T, Giannetti V, Leporini A, Saravia M M and Andrenucci M 2017 Influence of the magnetic field configuration on the plasma flow in Hall thrusters *Plasma Phys. Control. Fusion* **60** 014015
- [31] Marín-Cebrián A, Bello-Benítez E, Ahedo E and Domínguez-Vázquez A 2024 Kinetic electron effects in a Hall thruster discharge with a curved magnetic field topology *38th Int. Electric Propulsion Conf. (Toulouse, France, 23–28 June 2024)* (IEPC-2024-387) (Electric Rocket Propulsion Society)
- [32] Birdsall C K and Langdon A B 1991 *Plasma Physics via Computer Simulation* (Institute of Physics Publishing)
- [33] Domínguez-Vázquez A, Cichocki F, Merino M, Fajardo P and Ahedo E 2018 Axisymmetric plasma plume characterization with 2D and 3D particle codes *Plasma Sources Sci. Technol.* **27** 104009
- [34] Biagi S F 2004 Cross sections extracted from PROGRAM MAGBOLTZ, version 7.1 june 2004 (Accessed 5 July 2021)
- [35] Intel® 2023 oneMKL PARDISO - Parallel Direct Sparse Solver Interface (available at: [www.intel.com/content/www/us/en/docs/onemkl/developer-reference-c/2023-1/onemkl-pardiso-parallel-direct-sparse-solver-iface.html](http://www.intel.com/content/www/us/en/docs/onemkl/developer-reference-c/2023-1/onemkl-pardiso-parallel-direct-sparse-solver-iface.html))

- [36] Domínguez-Vázquez A, Zhou J, Sevillano-González A and Ahedo E 2025 Modelling of a Hall thruster plume: influence of plume boundary conditions and size and cathode location *Plasma Sources Sci. Technol.* **34** 085004
- [37] Marín-Cebrián A, Domínguez-Vázquez A, Fajardo P and Ahedo E 2021 Macroscopic plasma analysis from 1D-radial kinetic results of a Hall thruster discharge *Plasma Sources Sci. Technol.* **30** 115011
- [38] Gawron D, Mazouffre S, Sadeghi N and Héron A 2008 Influence of magnetic field and discharge voltage on the acceleration layer features in a Hall effect thruster *Plasma Sources Sci. Technol.* **17** 025001
- [39] Hargus W A and Nakles M R 2008 Ion velocity measurements within the acceleration channel of a low-power Hall thruster *IEEE Trans. Plasma Sci.* **36** 1989–97
- [40] Mazouffre S, Kulaev V and Pérez Luna J 2009 Ion diagnostics of a discharge in crossed electric and magnetic fields for electric propulsion *Plasma Sources Sci. Technol.* **18** 034022
- [41] Perrotin T, Vinci A E, Mazouffre S, Navarro-Cavallé J, Fajardo P and Ahedo E 2023 Measurements of xenon ions and atoms velocity in cylindrical Hall thruster with laser-induced fluorescence spectroscopy *10th EUCASS Conf., (Lausanne, Switzerland, 9–13 July 2023)*
- [42] Ahedo E, Gallardo J M and Martínez-Sánchez M 2003 Effects of the radial-plasma wall interaction on the axial Hall thruster discharge *Phys. Plasmas* **10** 3397–409
- [43] Bello-Benítez E and Ahedo E 2023 Stationary axial model of the Hall thruster plasma discharge: electron azimuthal inertia and far plume effects *Plasma Sources Sci. Technol.* **32** 115011
- [44] Poli D, Bello-Benítez E, Fajardo P and Ahedo E 2023 Time-dependent axial fluid model of the Hall thruster discharge and its plume *J. Phys. D: Appl. Phys.* **56** 415203
- [45] Hazeltine R D and Meiss J D 1992 *Plasma Confinement* (Addison-Wesley)
- [46] Ramos J J 2005 Fluid formalism for collisionless magnetized plasmas *Phys. Plasmas* **12** 052102
- [47] Charoy T, Lafleur T, Tavant A, Chabert P and Bourdon A 2020 A comparison between kinetic theory and particle-in-cell simulations of anomalous electron transport in ExB plasma discharges *Phys. Plasmas* **27** 063510
- [48] Jubin S, Powis A T, Villafana W, Sydorenko D, Rauf S, Khrabrov A V, Sarwar S and Kaganovich I D 2024 Numerical thermalization in 2D pic simulations: practical estimates for low-temperature plasma simulations *Phys. Plasmas* **31** 023902